Observation of anomalous nonequilibrium terahertz dynamics and a gapped topological phase in a semimetal $CaIrO_3$ thin film

K. Santhosh Kumar,* Monu Kinha,* Anagha P., Rahul Dagar, Siddharth Sharma, Dasarath Swaraj, and D. S. Rana†
Indian Institute of Science Education and Research, Bhopal 462066, Madhya Pradesh, India

(Received 2 January 2024; accepted 6 March 2024; published 25 March 2024)

Understanding the effects of coexisting electron correlations and spin-orbit coupling on the electronic ground state is the crux of emergent quantum phenomena in complex oxide systems. Here, we explore the critical role of such host interactions on the semimetallic state in $CaIrO_3$ epitaxial thin film using steady-state and time-resolved terahertz (THz) spectroscopies, and dc magneto transport measurements. We observe a THz optical gap of ∼1.6 meV in the Dirac bands along with a theoretically predicted topological semimetallic phase. The ultrafast dynamics of this gapped semimetallic phase, as studied by an optical-pump THz-probe tool, reveal a gigantic change in transmission that is unusual for a metal but typical of an insulating phase. As observed, this photoinduced change in THz transmission in the semimetallic phase of $CaIrO_3$ (bandgap of a few meV) is of the same order as in the insulating phase of other correlated perovskites having a bandgap of a few eV. An extremely slow recovery time compared to that of metals and other Dirac semimetallic compounds is another anomalous feature. These observations along with anisotropy in THz optical conductivity and dc magnetoconductance along the in-plane [100] and [010] crystal axes, place $CaIrO_3$ in a new category. This unprecedented combination of ultrafast THz dynamical properties provides valuable insights into the unified control of electron correlations and strong spin-orbit coupling in $CaIrO_3$, along with new room-temperature ultrafast THz modulation functionalities.

DOI: 10.1103/PhysRevB.109.115150

I. INTRODUCTION

The delicate interplay of host interactions such as electron correlations and spin-orbit coupling (SOC), and spatial or nonspatial symmetry-driven topological semimetals have renewed enormous scientific interest in the field of condensed matter physics due to their gapless states and unconventional properties [1,2]. In quest of such topologically nontrivial phases, the extensive experimental and theoretical studies suggest a topological semimetal as the linear band crossing at a point node or along a line with Dirac/Weyl type, which is responsible for the unique physical properties [2–6]. For example, Dirac semimetals exhibit giant magnetoresistance with maximum carrier mobility up to $9 \times 10^6\,\mathrm{cm}^2/\mathrm{V\,s}$, and negative MR, anomalous Hall effect, and Kerr rotation are observed for the chiral fermions in Weyl semimetals [3,7]. These unconventional physical properties are the way to a realization of dissipationless electronics and spintronics devices. Apart from their potential applications, topological band crossing gives rise to a variety of exotic phenomena such as intrinsic anomalous Hall effect, exotic surface states, large thermopower, and unusual responses related to quantum anomalies, which makes these compounds interesting from a fundamental point of view [3,8–12]. In addition, these topological semimetals are fertile grounds to realize the high-energy particles in condensed matter systems [1,2]. However, until today, the realization of topological phases, particularly in complex correlated oxides, and the origin of such unconventional physical properties are missing in the literature.

In this motive, the complex oxides $AIrO_3$ (A = Sr, Ca) with *Pbnm* space group are a promising class of materials to explore the topological semimetallic phase with entangled electron correlations and strong SOC [13–17]. Density functional theory calculations and group theory analysis predicted that $AIrO_3$ systems are Dirac nodal-line semimetals protected by crystalline symmetries [13,15]. However, the enhanced electron correlations in $CaIrO_3$ (CIO) due to small cation size resulting in large octahedral distortions push it to the Mott borderline, which is observed in dc transport properties [18,19]. Nonetheless, recently, the observation of the largest carrier mobility among the oxide semiconductors, $\sim 60\,000\,\mathrm{cm}^2/\mathrm{V}^{-1}\,\mathrm{s}^{-1}$, and giant magnetoresistance indicate the Dirac semimetal phase in CIO [5]. Also, Hall transport measurements support the presence of zero-bandgap Dirac states in CIO, which are robust against the epitaxial strain [20]. Despite this evidence, the investigation of low-energy carrier dynamics of the order of meV is missing in the literature to assure the gapless states in CIO, which is the limiting case for angle-resolved photoemission spectroscopy and density functional theory. In addition to that, the critical role of host interactions, such as electron correlations and SOC, in ground state formation is not completely understood.

In the past few decades, the eminence of terahertz (THz) spectroscopy in accessing the low-energy carrier dynamics near the Fermi level without strong modulations of interband transitions has been increasing progressively. Here, we have investigated the temperature-dependent THz optical

*These authors contributed equally to this work.
†dsrana@iiserb.ac.in

properties of CIO thin film on $(LaAlO_3)_{0.3}(Sr_2TaAlO_6)_{0.7}$ (LSAT) substrate along the two orthogonal in-plane directions [100] and [010] using time-domain THz spectroscopy. The optical excitationlike structure in THz optical conductivity and dielectric constant along both the pseudocubic in-plane directions suggest the gapped nature of Dirac bands. It further indicates that the CIO is a semimetal with an energy gap of around 1.6 meV. Further, the semiconductorlike behavior is verified using time-resolved THz spectroscopic measurements, which is different from other semimetallic compounds such as graphene. Finally, we evaluated the anisotropy in THz optical conductivity using dc magnetoconductance measurements and provided valuable information about the critical role played by SOC in CIO.

II. EXPERIMENTAL DETAILS

Polycrystalline CIO was prepared by the solid-state reaction route. CIO thin film was deposited on (100)-oriented LSAT substrate using a KrF excimer laser of wavelength 248 nm. Deposition parameters were optimized as follows: fluence, 2 J/cm^2; repetition rate, 2 Hz; and pressure, 10 Pa. Structural properties of epitaxial thin films were characterized using a PANalytical Empyrean x-ray diffractometer equipped with a two-bounce hybrid monochromator and an open four Euclidean cradle with Cu $K\alpha$ radiation. dc resistivity measurements were performed using the four-probe method on the physical property measurement system (Quantum Design). Optical properties in the 0.2–1.4 THz range were measured on the photoconductive antenna-based THz time-domain spectrometer in the transmission geometry and equipped with a helium closed loop cycle cryostat. The following procedure was used to acquire the highly reliable THz data without phase error. In the first step, the substrate was annealed in the same environment as optimized for the thin film in the pulsed laser deposition chamber and performed the temperature-dependent THz measurements on it. In the second step, THz measurements were performed on a thin film deposited on the same substrate. Finally, a complex refractive index of thin film was extracted with the help of Fresnel's equations, by taking temperature-dependent substrate THz measurements as a reference [21]. Nonequilibrium carrier dynamics of CIO thin film were performed on a home-built time-resolved THz spectrometer [22].

III. RESULTS AND DISCUSSIONS

A. Structural characterization

The x-ray diffraction θ-2θ scan of the CIO thin film is shown in Fig. 1(a), which indicates that the grown film on LSAT (100) is crystalline and phase pure. To get the information about the surface morphology, we have done the x-ray reflectivity measurement on CIO thin film, as shown in Fig. 1(b), along with best fit using X'PERT software reflectivity. Oscillations in the reflectivity data indicate the high quality of the thin film. The surface roughness was obtained as 0.5 nm from the fitting. To calculate the in-plane lattice constants, we have done the reciprocal space mapping (RSM) measurements along the (103) and (013) directions of the LSAT substrate shown in Figs. 1(c) and 1(d), respectively. The coherent thin film peaks with the LSAT substrate, as per RSM results revealing that the film is in the tetragonal symmetry.

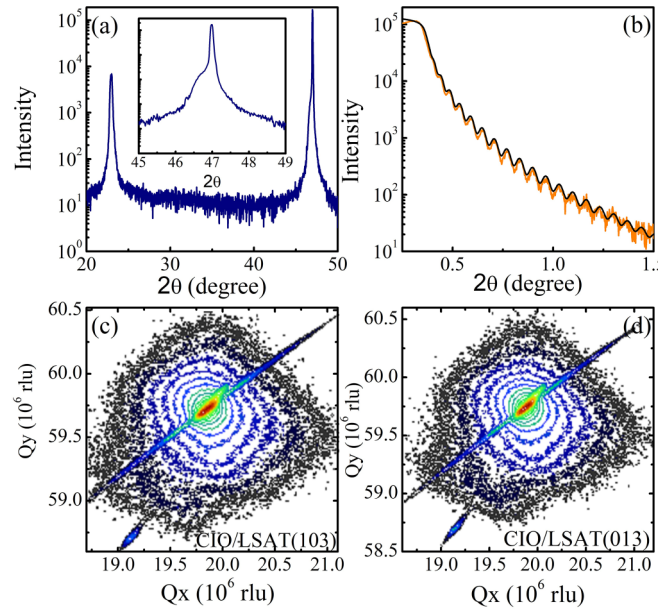

FIG. 1. (a) Shows the XRD θ-2θ scan of CIO thin film deposited on LSAT (100) substrate. The inset shows the zoomed view around the (200) peak. (b) X-ray reflectivity of the CIO thin film along with fitting. (c) and (d) show the reciprocal space maps of CIO thin film along Bragg reflection peaks (103) and (013) of the LSAT (100) substrate, respectively.

B. Terahertz spectroscopic measurements

Figures 2(a) and 2(c) show the temperature-dependent THz conductivity (σ_1^{100}) and THz dielectric constant (ε_1^{100}) of CIO/LSAT (100) thin film along the [100] direction at various frequencies, respectively. The σ_1^{100} exhibits nearly temperature-independent behavior, whereas the semiconductinglike behavior was observed in the dc electrical resistivity along the [100] direction [see inset of Fig. 2(b)]. However, the subtle change in slope near 100 K for resistivity followed by a humplike signature in σ_1^{100} at higher frequencies was observed. The ε_1^{100} is ∼300 at low temperatures and decreases as the temperature increases. Also, the decrease in ε_1^{100} is sharp at around 100 K. At high frequencies, the ε_1^{100} shows the zero crossover around 100 K, which is similar to the dielectric response at the insulator-metal transition. However, the temperature dependence of conductivity (σ_1^{010}) along the [010] direction is distinct from σ_1^{100}. The σ_1^{010} increases with temperature and its magnitude is high in comparison to σ_1^{100} [see Fig. 2(b)]. The semiconductinglike behavior of σ_1^{010} is consistent with the dc electrical resistivity, as shown in the inset of Fig. 2(b). Surprisingly, in contrast to the THz optical response, dc electrical resistivity along both in-plane directions is nearly similar except for the magnitude (the ratio of dc resistivity $\rho_{100}/\rho_{010} \sim 1.2$) [see the inset of Fig. 2(b)]. Further, the temperature dependence of ε_1^{100} and ε_1^{010} are also distinct from each other. ε_1^{010} is positive except at a frequency of 0.2 THz and exhibits an oscillating type of behavior with temperature [see Fig. 2(d)]. To surmise, the

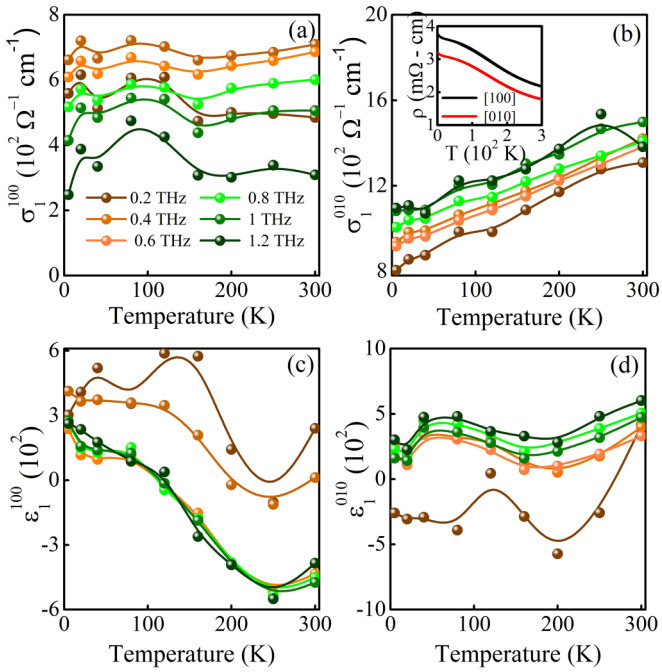

FIG. 2. Shows the temperature-dependent optical properties of CIO/LSAT (100) thin film along two orthogonal in-plane directions. (a),(c) and (b),(d) show the temperature-dependent optical conductivity and dielectric constant along the [100] and [010] directions at various frequencies, respectively. Inset in (b) represents the temperature-dependent dc electrical resistivity along both in-plane directions.

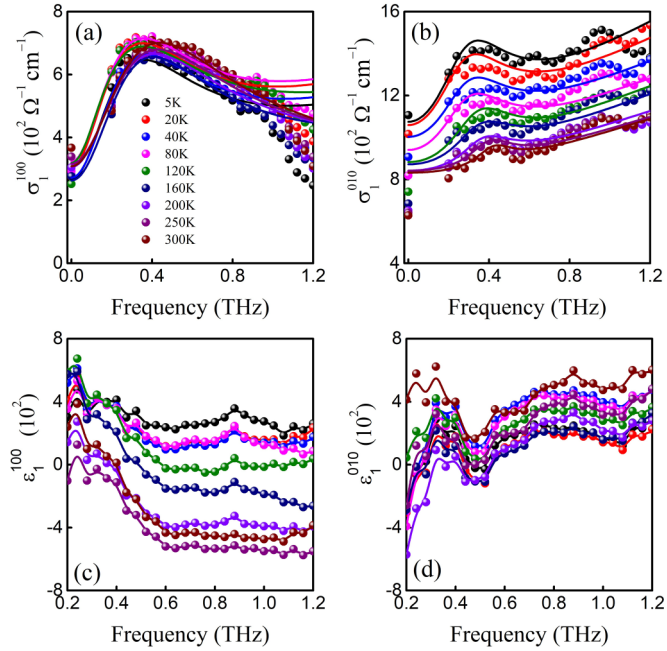

FIG. 3. Frequency-dependent optical properties of CIO/LSAT (100) thin film along orthogonal in-plane directions. (a),(c) and (b),(d) represent the frequency-dependent optical conductivity and dielectric constant along in-plane directions [100] and [010] at various temperatures, respectively. dc conductivity obtained using the four-probe method is shown at zero frequency. The optical conductivity is fitted with a sum of the Drude-Smith+Lorentz model as explained in the main text.

temperature-dependent THz conductivity and THz dielectric constant show significant anisotropy along both the in-plane directions [100] and [010] in CIO thin film.

The THz optical anisotropy can be understood in terms of epitaxial strain. The orthorhombic CIO thin film deposited on the LSAT substrate is constrained by the epitaxial relation $a_o^2 + b_o^2 = (2a_{\mathrm{LSAT}})^2$. It results in 2.2% tensile and 2.1% compressive epitaxial strain along both in-plane directions, respectively. This structural constraint leads to a distorted metastable tetragonal phase with distinct octahedral rotations around perpendicular in-plane directions. This asymmetry in octahedra rotations affects the bond lengths and bond angles, which leads to changes in orbital overlap along both crystallographic directions. Since CIO is close to the Mott borderline, the epitaxial strain impacts effectively and results in transport anisotropy. However, the subpicosecond timescale electrodynamics exhibit discernible anisotropy compared to the dc transport properties. This could be due to the fact that dc transport is sensitive to large-angle momentum relaxing scattering processes, whereas optical transport includes the momentum-conserving scattering as well when the Galilean invariance is broken by lattice or SOC [23]. Therefore, SOC can play a notable role in giving rise to the optical anisotropy as SOC is inherent in iridium materials.

The THz optical properties of CIO/LSAT (100) thin film along the two pseudocubic in-plane orientations at various temperatures are shown in Fig. 3. The frequency-dependent σ_1^{100} shows an optical excitationlike mode around ∼0.4 THz [see Fig. 3(a)]. The dielectric constant ε_1^{100} shows a dispersion at low frequencies due to an optical excitation and is frequency independent at high frequency, whereas ε_1^{010} is nearly frequency independent at all temperatures [see Figs. 3(c) and 3(d)]. The optical excitation is consistent in σ_1^{010} and ε_1^{010}, and the high frequency σ_1^{010} increases with frequency, which is in contrast with σ_1^{100} [see Figs. 3(b) and 3(d)]. Here, we have used geometrical factors 0.8 and 2 to match the THz conductivity along the [100] and [010] directions, respectively. However, ε_1^{100} and ε_1^{010} are similar with low-frequency dispersion and frequency-independent nature at high frequency. Since the conductivity along both directions indicates an optical excitationlike mode modulated by free carrier dynamics, we have modeled the complex conductivity using the Drude-Smith+Lorentz model as expressed in Eq. (1) [24].

$$\sigma(\omega) = \frac{\omega_{\mathrm{pL}}^2}{4\pi}\frac{\omega}{\omega\tau_{\mathrm{L}} + i\left(\omega_0^2 - \omega^2\right)} + \frac{\omega_{\mathrm{pDS}}^2}{4\pi}\frac{\tau_{\mathrm{DS}}}{(1 - i\omega\tau_{\mathrm{DS}})} \times \left[1 + \sum_{n=1}^{\infty}\frac{c_n}{(1 - i\omega\tau)^n}\right] - i\varepsilon_0\omega(\varepsilon_\infty - 1). \quad (1)$$

Here, the subscripts "L" and "DS" represent Lorentz and Drude-Smith, respectively. ω_{p} is the plasma frequency, τ is relaxation time, and ω_0 is the excitation frequency. c_n is the fraction of carriers that retains the original velocity after the nth collision and $c = -1$ refers to a fully backscattered state or a localized state and shifts the zero-frequency maximum to finite frequency. Lattice contribution to the conductivity

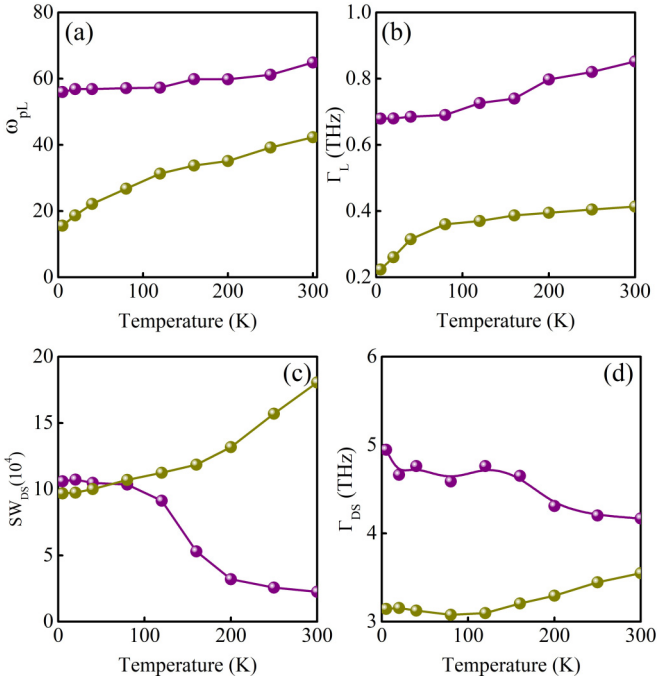

FIG. 4. Temperature-dependent fitting parameters of the THz complex optical conductivity along both in-plane directions. (a) and (b) show the strength of the optical excitation mode (ω_{pL}) and the linewidth (Γ_L) as a function of temperature, respectively. (c) and (d) show the SW_{DS} (ω^2_{pDS}) and scattering rate (Γ_{DS}) of the free carriers as a function of temperature, respectively. Dark yellow and purple colors correspond to the two in-plane orientations [100] and [010], respectively.

is $-i\varepsilon_0\omega(\varepsilon_\infty - 1)$ [21]. The simultaneous fits to the THz conductivity are reasonably matched with the dc conductivity. The dynamical optical parameters obtained from optical conductivity fitting are plotted in Fig. 4 as a function of temperature. The optical conductivity is fitted with an optical excitation mode at a frequency of ∼0.4 and ∼0.3 THz along both the in-plane [100] and the [010] directions, respectively. In general, these types of optical excitationlike modes in the THz frequency regimes can have several origins. However, the magnetic origin of this mode can be discarded safely owing to the paramagnetic nature of CIO. Apart from this, optical phonon modes in $AIrO_3$ (A=Sr, Ca) and other similar systems lie well above 2 THz, further negating the possibility of the existence of the observed optical excitationlike mode due to the optical phonons [25–30].

To understand a THz optical conductivity spectrum and evaluate the electronic contribution, we have performed a group theory analysis on CIO with *Pbnm* space group. CIO possesses one electron with spin-1/2 and T and P symmetries. In the presence of SOC, the composite symmetry Θ is defined as $P * T$ and $\Theta^2 = -1$ ensures the Krammer's pair degeneracy in the entire momentum space. Let us consider the $k_b = \pi$ plane, which is invariant under the n-glide plane (G_n) operation. The eigenvalues of the G_n are derived as $G_n^2 = -e^{i(k_a+k_c)}$. Here, the "−" sign denotes the 2π rotation in the spin space. Therefore, the eigenvalues of G_n: $n_\pm = \pm ie^{(ik_a+ik_c)/2}$, serve as quantum numbers of Bloch states in the entire $k_b = \pi$ plane. Other symmetries present on this plane act as a little group of the Hamiltonian to represent the Bloch states. Since both G_n and the screw axis S_a are present at the U point $(0, \pi, \pi)$ in the Brillouin zone, the eigenstates can be written as a combination of them. The eigenvalues of the screw axis are $a_\pm = \pm ie^{ik_a/2}$ ($S_a^2 = -e^{ik_a}$). Therefore, the complete set of simultaneous eigenstates in the presence of a b-glide plane (G_b) are

$$G_nG_b = -e^{ik_a-ik_b}G_bG_n \rightarrow [G_n, G_b] = 0 \text{ (at } U \text{ point)}, \quad (2)$$

$$G_n(G_b|n_+\rangle) = G_b(G_n|n_+\rangle) = n_+(G_b|n_+\rangle). \quad (3)$$

At the U point, G_b maps an a_+ state into an a_- state and vice versa.

$$G_bS_a = e^{-ik_a+ik_b}S_aG_b \rightarrow \{G_b, S_a\} = 0 \text{ (at } U \text{ point)}, \quad (4)$$

$$S_a(G_b|a_+\rangle) = -G_b(S_a|a_+\rangle) = -a_+(G_b|a_+\rangle) = a_-(G_b|). \quad (5)$$

Since n_+/n_- states remain the same under the G_b, they no longer coexist in a single state. Therefore, simultaneous eigenstates at the U point can be written as two sets: $\{|n_+, a_+\rangle, |n_+, a_-\rangle, \Theta|n_+, a_+\rangle, \Theta|n_+, a_-\rangle\}$ and $\{|n_-, a_+\rangle, |n_-, a_-\rangle, \Theta|n_-, a_+\rangle, \Theta|n_-, a_-\rangle\}$. As the bands evolve towards the Brillouin zone boundaries along the R-S line,

$$G_nG_b = -e^{ik_a-ik_b}G_bG_n \rightarrow \{G_n, G_b\} = 0, \quad (6)$$

$$\begin{aligned} G_n(G_b|n_+, a_+\rangle) &= -G_b(G_n|n_+, a_+\rangle) \\ &= -n_+(G_b|n_+, a_+\rangle) \\ &= -n_-(G_b|n_+, a_+\rangle). \end{aligned} \quad (7)$$

The n_+ state maps into the n_- state under the anticommutation relation of G_n and G_b. Therefore, it clearly indicates a G_n partner exchange along the path from the U point to the R-S line. A similar argument is valid from the U point to the S-X line: the n_+ state maps into the n_- state under the anticommutation relation of G_n and S_a, which ensures the coexistence of n_+ and n_- in an eigenstate. These constraints enforce a fourfold Dirac nodal ring on the $k_b = \pi$ plane with the U point as center [31,32].

In addition, the presence of Dirac-like dispersion around the U point ($k_a = 0$, $k_b = \pi$, $k_c = \pi$) in the Brillouin zone was also confirmed by density functional theory calculations, angle-resolved photoemission spectroscopy measurements, and THz spectroscopic measurements [33–35]. This linear dispersion is sensitive to crystal symmetries and electron correlations. A clear energy gap of ∼5 meV is seen in the linear Dirac bands upon breaking the crystal symmetry in $SrIrO_3$ [33]. Further, the linear dispersion in CIO is close to the Fermi level, around ∼8 meV below E_F, and is very sensitive to electron correlations [5]. The increased octahedra rotations due to the smaller cation size and epitaxial strain in CIO can significantly enhance the electron correlations that lead to opening a gap in Dirac states. Therefore, we attribute this mode to an optical excitation across the gap in the upper and lower Dirac cones.

The energy gap [$\Delta = \omega_0$ (meV)] of 1.65 and 1.25 meV along the [100] and [010] directions show subtle changes with temperature. The strength of the mode (ω_{pL}) increases with

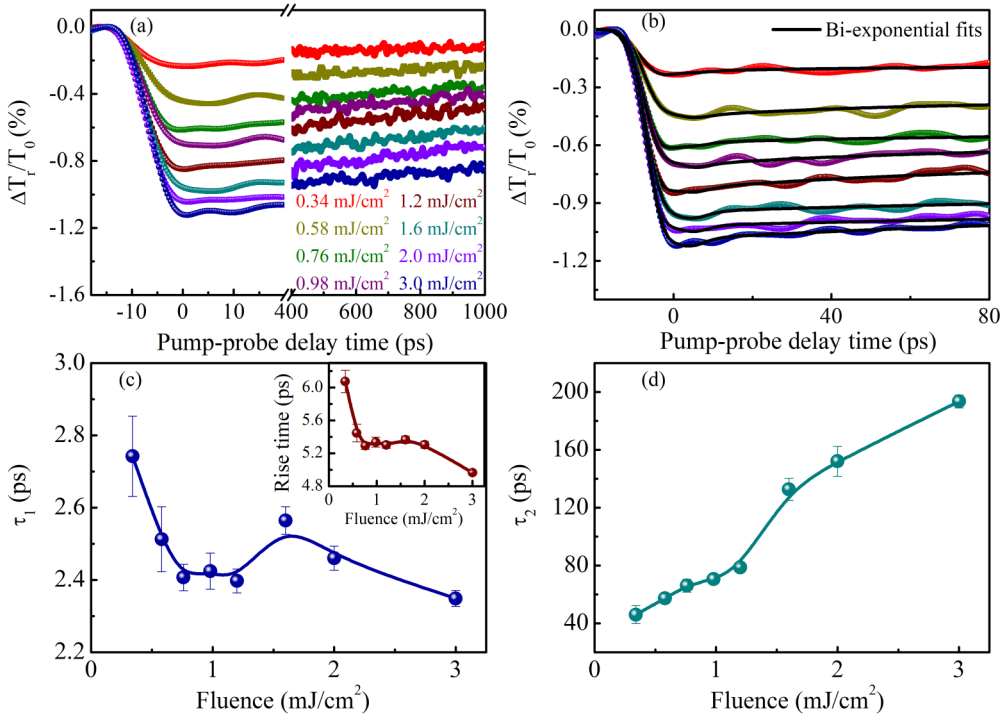

FIG. 5. (a) and (b) show the transient THz transmission change as a function of pump-probe delay time at various optical-pump fluence at longer and shorter timescales, respectively. Black line in (b) represents the biexponential fits to the experimental data. (c) and (d) show the obtained relaxation time constants by fitting the biexponential function to transient THz transmission change, as a function of optical-pump fluence. The inset in (c) shows the obtained rise time as a function of optical-pump fluence. The lines joining the data points in (c), (d), and the inset are guides to the eyes.

temperature, as shown in Fig. 4(a). It indicates that the thermally excited carriers are contributing as the optical gap lies well below the room-temperature thermal energy (25 meV) [25–30]. Further, the linewidth ($\Gamma_L = 1/\tau_L$) of the mode increases with temperature suggesting the thermal broadening of the mode [see Fig. 4(b)]. The ω_{pL} and Γ_L follow a similar trend along both in-plane directions, albeit with subtle changes in magnitude. Overall, our THz conductivity dynamics suggest that CIO is a gapped semimetal. As the energy gap (Δ) is very small, it might remain elusive in theoretical calculations and angle-resolved photoemission spectroscopy measurements.

Furthermore, in addition to the linearly dispersing electron band, a flat holelike band at $(0,\pm\pi)$ and $(\pm\pi,0)$ were observed in the electronic structure of its sister compound $SrIrO_3$ [34,35]. Therefore, the optical response is modulated by the hole carrier response in THz conductivity. To account for these contributions, additional Drude/Drude-Smith models are sufficient, which is a common approach in multiband systems [21,24]. However, incorporating more terms into the model may lead to ambiguities in the determination of optical fitting parameters. Hence, we considered a single Drude-Smith model to account for the hole carrier response. The spectral weight ($SW_{DS} = \omega^2_{pDS}$) of the free carrier response considered from the Drude-Smith model is plotted in Fig. 4(c). SW_{DS} along the [100] direction increases with temperature while the scattering rate ($\Gamma_{DS} = 1/\tau_{DS}$) is comparatively small and shows an increasing trend with temperature [see Figs. 4(c) and 4(d)]. The temperature-dependent SW_{DS} is consistent with the semiconductinglike dc electrical resistivity. In addition, a slightly enhanced Γ_{DS} suggests that the thermally excited carriers are contributing to spectral weight—probably, Dirac electrons. However, the SW_{DS} along the [010] direction decreases with increasing temperature, which is a typical correlated metal behavior. In contrast to the SW_{DS}, Γ_{DS} drastically decreases with temperature along the [010] direction. The distinct THz electrodynamics of carriers along the in-plane directions are responsible for the anisotropy in THz conductivity.

Further, to confirm the gapped nature and to understand the nonequilibrium carrier dynamics of CIO/LSAT (100) thin film, we performed time-resolved terahertz spectroscopic measurements. Figure 5 shows the transient terahertz dynamics of CIO thin film under 800 nm optical-pump excitation at a range of optical-pump fluences. Here, $\Delta T_r = T(t) - T_0$, where T_0 and $T(t)$ correspond to the maximum transmitted THz amplitude without photoexcitation and transmitted THz amplitude as a function of pump-probe delay time (t) after photoexcitation, respectively. Thus, ΔT_r corresponds to the change in the transmitted THz amplitude upon photoexcitation. The observed transient THz transmission change is negative, which is a typical signature of semiconductinglike behavior and contrasts with the observed increase in THz transmission for Dirac semimetal graphene [36]. THz transmission is decreasing with increasing optical-pump fluence, suggesting the enhanced number of photocarriers in the conduction band, which is a typical behavior of semiconductors.

However, this decrease in THz transmission upon photoexcitation is in accordance with other perovskite semiconducting type materials such as manganites, nickelates, etc., which

is interesting from the viewpoint that these materials have bandgaps in the range of a few eV and CIO has a bandgap of the order of a few meV [22,37,38]. The recovery time of transient THz transmission is slow and beyond our experimental window—probably, in the nanosecond timescale. Nonetheless, the THz transmission decreases at a slow rate compared to metals and other Dirac semimetallic compounds. The observed slow rise time cannot solely be explained on the basis of the setup resolution and, thus, is inherent to the material itself [39]. Overall, the transient THz dynamics indicate a semiconductorlike behavior rather than the expected Dirac semimetal, which is consistent with the corroboration of ground state THz conductivity dynamics (see Figs. 3 and 4).

To gain further insights into the nonequilibrium carrier dynamics, we fitted the transient THz transmission change with a biexponential function as expressed below:

$$\frac{\Delta T_r}{T_0}(t) = 0.5 * \mathrm{erf}\left(\frac{t}{\tau_c}\right) * \left[A * \exp\left(-\frac{t}{\tau_1}\right) + B * \exp\left(-\frac{t}{\tau_2}\right) + C\right], \tag{8}$$

where the parameters A and B correspond to the amplitudes of the two relaxation time constants, C is the constant offset, while τ_1 and τ_2 correspond to the two relaxation time constants, and τ_c is ascribed to the rise time. The biexponential fits are shown as black lines in Fig. 5(b). The obtained relaxation time constants are plotted in Figs. 5(c) and 5(d) as a function of optical-pump fluence. The rise time is ∼6 ps at the fluence of ∼0.34 mJ/cm^2 and decreases as the optical-pump fluence increases [see inset of Fig. 5(c)]. The obtained two relaxation time constants show the opposite trend, while one decreases with an increase in optical-pump fluence and the other one increases with an increase in optical-pump fluence [see Figs. 5(c) and 5(d)].

The observed semiconductorlike behavior upon photoexcitation implies that the carrier generation upon photoexcitation plays a dominant role over the carrier-carrier scattering. This relaxation scenario is different from the temperature dissipation via the electron-phonon scattering process, which is widely reported in metals, graphene, and highly doped semiconductors. The relaxation has been explained on the basis of a two-temperature model [36,40]. Recently, the Rothwarf-Taylor (RT) model was employed to address the ultrafast relaxation dynamics of gapped Dirac semimetallic Cd_3As_2 thin film [41,42]. The formation of an energy gap was shown to hamper the relaxation of quasiparticles (QPs), thus, prolonging the recovery process via the phonon bottleneck effect. The phonon bottleneck effect is caused by the generation of high-frequency phonons, which are generated when the recombination of the QPs takes place across the energy gap, further reexciting the recombined charge carriers, which prolongs the recovery process of the entire system [43]. On a similar note, owing to the gapped nature of topological CIO thin film corroborated by steady-state THz measurements and theoretical calculations, the observed relaxation dynamics can be explained on the basis of the RT model and are ascribed to the electron-hole recombination arbitrated by phonon-phonon scattering [44].

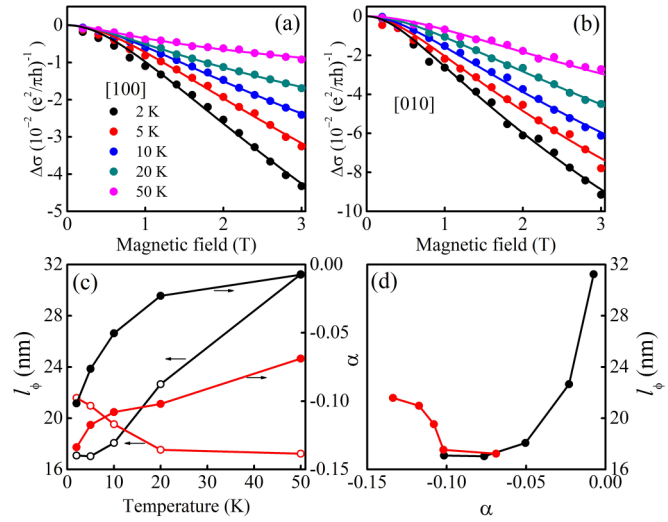

FIG. 6. (a) and (b) show the magnetoconductance ($\Delta\sigma$) as a function of applied magnetic field at various temperatures along both in-plane directions [100] and [010], respectively. The solid lines in (a) and (b) are the simplified HLN equation fitting to the experimental data. (c) shows the temperature-dependent phase coherence length (l_ϕ) and spin-orbit coupling strength (α); (d) shows the correlation between phase coherence length (l_ϕ) and spin-orbit coupling strength (α) along both in-plane directions. The black and red colors in (c) and (d) indicate the [100] and [010] directions, respectively.

Upon photoexcitation, intraband scatterings such as carrier-phonon and carrier-carrier scattering result in the redistribution of electrons and holes in the conduction and valence bands and are governed by the rise time of the transient THz transmission change. Subsequently, the relaxation dynamics are ascribed to the electron-hole recombination and the anharmonic coupling of optical phonons to other uncoupled phonons, such as acoustic phonons [44]. It has been theoretically predicted that the decay time constants associated with acoustic phonons around the Dirac point lie on the order of microseconds, and it decreases to nanoseconds in the case of heavily doped samples [45]. So, the observed decay time constants on the order of a nanosecond can be attributed to the coupling of acoustic phonons scattering. The repopulation of electrons and holes in their respective bands occurs due to the excitation of high-frequency phonons or these high-frequency phonons dissociating into low-frequency phonons; both these processes prolong the recovery process. Overall, the observed disparity in the nonequilibrium carrier dynamics in CIO thin film in comparison to other Dirac semimetallic compounds could be due to the presence of an optical gap in the presence of both electron correlations and spin-orbit coupling.

To understand the transport anisotropy in THz conductivity and to gain more insights into the carrier scattering mechanism, we have obtained the magnetoconductivity along both the in-plane directions. Figure 6 shows the magnetotransport properties of the CIO thin film along the in-plane directions [100] and [010]. The magnetoconductance as a function of the magnetic field at various temperatures is shown in Fig. 6(a)

for the [100] direction. Surprisingly, we observed the negative magnetoconductance, which was observed in graphene, strongly spin-orbit coupled systems, topological insulators, etc. [46]. Generally, the negative magnetoconductance is the signature of a weak antilocalization effect, which is different from the conventional localization in 2D systems and Mott materials. Weak antilocalization arises due to the destructive interference of coherently backscattered electrons spin rotation in the presence of SOC. To obtain the important information, we analyzed the experimental data using the Hikami-Larkin-Nagaoka (HLN) equation. Since CIO is close to the Mott borderline, we have considered the strong SOC limit in the HLN equation [46]. The experimental data well fits the HLN equation:

$$\Delta\sigma(B) = -\alpha\frac{e^2}{\pi h}\left[\ln\left(\frac{\hbar}{4el_\varphi^2 B}\right) - \Psi\left(\frac{\hbar}{4el_\varphi^2 B}\right)\right]. \quad (9)$$

The parameters $\Delta\sigma$, B, α, Ψ, $\hbar$, e, and l_φ correspond to the magnetoconductivity, magnetic field, prefactor, digamma function, Planck's constant, electronic charge, and phase coherence length, respectively. The extracted parameters, such as prefactor and phase coherence length, are plotted as a function of temperature and magnetic field, respectively [see Figs. 6(c) and 6(d)]. The magnitude of α is small, indicating that the strength of weak antilocalization is low and slightly decreases with temperature along the [100] direction. Further, the maximum phase coherence length of 32 nm is obtained at 50 K and decreases as the temperature decreases for the [100] direction. However, along the [010] direction, the magnitude of α follows a similar trend, whereas l_φ is decreasing with increasing temperature. In general, l_φ is expected to decrease with temperature due to the dominant contribution of inelastic scattering. The behavior of l_φ is consistent with theoretical predictions along the [010] direction, while the opposite trend in [100] is quite surprising. Considering the role of electron correlations in CIO, the observed small value of l_φ could possibly be due to the strong electron correlations and reduced screening effects due to the low carrier density at the Fermi level. X-ray photoemission spectroscopy on the same film provides evidence for low carrier density at the Fermi level [47]. The correlation plot between α and l_φ also shows the contrast behavior along the two in-plane directions, as shown in Fig. 6(d). Since CIO is at the correlated Mott borderline, from magnetotransport results, we believe that the spin-orbit coupling is responsible for the negative magnetoconductivity, and electron correlations shorten the phase coherence length. The anisotropy in l_φ could be the possible cause of anisotropy in optical parameters, as shown in Figs. 4(c) and 4(d) along both in-plane directions. Further, it clearly indicates that the complex interplay of electron correlations and SOC is responsible for the anisotropy in CIO. Overall, our findings give valuable insights into the semimetallic state driven by the complex interplay of electron correlations and SOC in CIO.

IV. CONCLUSIONS

Here, we have studied the semimetallic state in CIO/LSAT (100) thin film using time-domain and time-resolved THz spectroscopy. The obtained ground state THz conductivity indicates an optical excitationlike feature modulated by free carrier response in CIO along both the in-plane [100] and [010] directions rather than the theoretically expected topological semimetallic state. To understand the THz electrodynamics, we performed a group theory analysis on parent orthorhombic CIO and attributed the optical excitationlike feature in THz conductivity to the gap in Dirac bands. The observed semiconductorlike behavior in ground state measurements is consistent with the observations in time-resolved THz spectroscopic measurements. Despite the small bandgap ($\sim$1.6 meV), the transient transmission change is of the order of transmission change in other perovskite semiconductors with a bandgap of a few eV such as manganites and nickelates. The recovery time of photoexcited carriers is slow compared to metals and other Dirac semimetallic compounds. Further, the anisotropy in THz optical conductivity along both in-plane directions is unraveled using magnetotransport measurements. The observed negative magnetoconductivity and shortened phase coherence length reveal the critical role of spin-orbit coupling and electron correlations, respectively. Overall, our findings provide insight into the dynamics of the system, which is useful for understanding the strong spin-orbit coupled systems.

ACKNOWLEDGMENTS

D.S.R. acknowledges the financial support from Science and Engineering Research Board (SERB), New Delhi under Project No. CRG/2020/002338.

[1] A. A. Burkov, Nat. Mater. **15**, 1145 (2016).
[2] Beyond particle physics, Nat. Mater. **15**, 1139 (2016).
[3] C. Shekhar, A. K. Nayak, Y. Sun, M. Schmidt, M. Nicklas, I. Leermakers, U. Zeitler, Y. Skourski, J. Wosnitza, Z. Liu, Y. Chen, W. Schnelle, H. Borrmann, Y. Grin, C. Felser, and B. Yan, Nat. Phys. **11**, 645 (2015).
[4] Z. K. Liu, J. Jiang, B. Zhou, Z. J. Wang, Y. Zhang, H. M. Weng, D. Prabhakaran, S.-K. Mo, H. Peng, P. Dudin, T. Kim, M. Hoesch, Z. Fang, X. Dai, Z. X. Shen, D. L. Feng, Z. Hussain, and Y. L. Chen, Nat. Mater. **13**, 677 (2014).
[5] J. Fujioka, R. Yamada, M. Kawamura, S. Sakai, M. Hirayama, R. Arita, T. Okawa, D. Hashizume, M. Hoshino, and Y. Tokura, Nat. Commun. **10**, 362 (2019).
[6] N. P. Armitage, E. J. Mele, and A. Vishwanath, Rev. Mod. Phys. **90**, 015001 (2018).
[7] T. Liang, Q. Gibson, M. N. Ali, M. Liu, R. J. Cava, and N. P. Ong, Nat. Mater. **14**, 280 (2014).
[8] G. S. Thakur, P. Vir, S. N. Guin, C. Shekhar, R. Weihrich, Y. Sun, N. Kumar, and C. Felser, Chem. Mater. **32**, 1612 (2020).
[9] B. Q. Lv, H. M. Weng, B. B. Fu, X. P. Wang, H. Miao, J. Ma, P. Richard, X. C. Huang, L. X. Zhao, G. F. Chen, Z. Fang, X. Dai, T. Qian, and H. Ding, Phys. Rev. X **5**, 031013 (2015).

[10] S.-Y. Xu *et al.*, Sci. Adv. **1**, e1501092 (2015).
[11] K. Ueda, R. Kaneko, H. Ishizuka, J. Fujioka, N. Nagaosa, and Y. Tokura, Nat. Commun. **9**, 3032 (2018).
[12] K. Sonowal, A. Singh, and A. Agarwal, Phys. Rev. B **100**, 085436 (2019).
[13] M. A. Zeb and H.-Y. Kee, Phys. Rev. B **86**, 085149 (2012).
[14] Y. Sun, Y. Zhang, C.-X. Liu, C. Felser, and B. Yan, Phys. Rev. B **95**, 235104 (2017).
[15] Y. Chen, Y.-M. Lu, and H.-Y. Kee, Nat. Commun. **6**, 6593 (2015).
[16] W. Witczak-Krempa, G. Chen, Y. B. Kim, and L. Balents, Annu. Rev. Condens. Matter Phys. **5**, 57 (2014).
[17] S. Bhowal and S. Satpathy, Phys. Rev. B **100**, 115101 (2019).
[18] A. Mauko, J. Fujioka, M. Nakamura, M. Kawasaki, and Y. Tokura, APL Mater. **7**, 081115 (2019).
[19] A. Biswas and Y. H. Jeong, J. Appl. Phys. **117**, 195305 (2015).
[20] D. Hirai, J. Matsuno, D. Nishio-Hamane, and H. Takagi, Appl. Phys. Lett. **107**, 012104 (2015).
[21] K. Santhosh Kumar, E. V. Phanindra, and D. S. Rana, Phys. Rev. B **100**, 125127 (2019).
[22] M. Kinha, G. L. Prajapati, M. Udeshi, P. Agarwal, N. B. Ram, and D. S. Rana, J. Phys. D: Appl. Phys. **55**, 225301 (2022).
[23] D. L. Maslov and A. V. Chubukov, Rep. Prog. Phys. **80**, 026503 (2017).
[24] S. Das, G. L. Prajapati, P. Anagha, and D. S. Rana, Phys. Rev. B **98**, 115110 (2018).
[25] D. N. Basov, R. D. Averitt, D. van der Marel, M. Dressel, and K. Haule, Rev. Mod. Phys. **83**, 471 (2011).
[26] D. N. Basov and T. Timusk, Rev. Mod. Phys. **77**, 721 (2005).
[27] K. Santhosh Kumar, G. L. Prajapati, R. Dagar, M. Vagadia, D. S. Rana, and M. Tonouchi, Adv. Opt. Mater. **8**, 1900958 (2019).
[28] R. Rana, P. Pandey, V. E. Phanindra, S. S. Prabhu, and D. S. Rana, Phys. Rev. B **97**, 045123 (2018); S. Das, G. L. Prajapati, and D. S. Rana, *ibid.* **102**, 214403 (2020).
[29] Z. Zhang, F. Y. Gao, J. B. Curtis *et al.*, Nat. Phys. (2024), doi:10.1038/s41567-024-02386-3.
[30] Z. Zhang, F. Y. Gao, Y.-C. Chien, Z.-J. Liu, J. B. Curtis, E. R. Sung, X. Ma, W. Ren, S. Cao, P. Narang, A. von Hoegen, E. Baldini, and K. A. Nelson, Nat. Phys. (2024).
[31] C. Fang, Y. Chen, H.-Y. Kee, and L. Fu, Phys. Rev. B **92**, 081201(R) (2015).
[32] Y. Chen, H.-S. Kim, and H.-Y. Kee, Phys. Rev. B **93**, 155140 (2016).
[33] K. Santhosh Kumar, A. P., C. Sun, and D. S. Rana, Phys. Rev. B **106**, 245135 (2022).
[34] Y. F. Nie, P. D. C. King, C. H. Kim, M. Uchida, H. I. Wei, B. D. Faeth, J. P. Ruf, J. P. C. Ruff, L. Xie, X. Pan, C. J. Fennie, D. G. Schlom, and K. M. Shen, Phys. Rev. Lett. **114**, 016401 (2015).
[35] P. Schütz, D. Di Sante, L. Dudy, J. Gabel, M. Stübinger, M. Kamp, Y. Huang, M. Capone, M.-A. Husanu, V. N. Strocov, G. Sangiovanni, M. Sing, and R. Claessen, Phys. Rev. Lett. **119**, 256404 (2017).
[36] Z. Y. Zhang, T. Lin, X. Xing, X. Lin, X. J. Meng, Z. X. Cheng, Z. M. Jin, and G. H. Ma, Appl. Phys. Lett. **110**, 111108 (2017).
[37] M. Kinha, M. Udeshi, R. Dagar, and D. S. Rana, J. Appl. Phys. **131**, 233103 (2022).
[38] B. Torriss, A. Ibrahim, T. Ozaki, and M. Chaker, Phys. Rev. B **98**, 165132 (2018).
[39] M. Y. Zhang, Z. X. Wang, Y. N. Li, L. Y. Shi, D. Wu, T. Lin, S. J. Zhang, Y. Q. Liu, Q. M. Liu, J. Wang, T. Dong, and N. L. Wang, Phys. Rev. X **9**, 021036 (2019).
[40] C. Voisin, N. Del Fatti, D. Christofilos, and F. Vallee, J. Phys. Chem. B **105**, 2264 (2001).
[41] W. Zhang, Y. Yang, P. Suo, W. Zhao, J. Guo, Q. Lu, X. Lin, Z. Jin, L. Wang, G. Chen, F. Xiu, W. Liu, C. Zhang, and G. Ma, Appl. Phys. Lett. **114**, 221102 (2019).
[42] A. Rothwarf and B. N. Taylor, Phys. Rev. Lett. **19**, 27 (1967).
[43] W. Zhang, Y. Yang, P. Suo, K. Sun, J. Peng, X. Lin, F. Xiu, and G. Ma, Phys. Rev. B **106**, 155137 (2022).
[44] W. Lu, J. Ling, F. Xiu, and D. Sun, Phys. Rev. B **98**, 104310 (2018).
[45] R. Lundgren and G. A. Fiete, Phys. Rev. B **92**, 125139 (2015).
[46] M. Jenderka, J. Barzola-Quiquia, Z. Zhang, H. Frenzel, M. Grundmann, and M. Lorenz, Phys. Rev. B **88**, 045111 (2013).
[47] K. Santhosh Kumar, B. H. Reddy, R. Dagar, R. S. Singh, and D. S. Rana, AIP Conf. Proc. **2115**, 030378 (2019).